A new function for a common fold: the crystal structure of quinolinic acid phosphoribosyltransferase

Janina C Eads[1], Derya Ozturk[2], Tom B Wexler[1], Charles Grubmeyer[2] and James C Sacchettini[1†*]

Background: Quinolinic acid (QA) is a neurotoxin and has been shown to be present at high levels in the central nervous system of patients with certain diseases, such as AIDS and meningitis. The enzyme quinolinic acid phosphoribosyltransferase (QAPRTase) provides the only route for QA metabolism and is also an essential step in *de novo* NAD biosynthesis. QAPRTase catalyzes the synthesis of nicotinic acid mononucleotide (NAMN) from QA and 5-phosphoribosyl-1-pyrophosphate (PRPP). The structures of several phosphoribosyltransferases (PRTases) have been reported, and all have shown a similar fold of a five-stranded β sheet surrounded by four α helices. A conserved sequence motif of 13 residues is common to these 'type I' PRTases but is not observed in the QAPRTase sequence, suggestive of a different fold for this enzyme.

Results: The crystal structure of QAPRTase from *Salmonella typhimurium* has been determined with bound QA to 2.8 Å resolution, and with bound NAMN to 3.0 Å resolution. Most significantly, the enzyme shows a completely novel fold for a PRTase enzyme comprising a two-domain structure: a mixed α/β N-terminal domain and an α/β barrel-like domain containing seven β strands. The active site is located at the C-terminal ends of the β strands of the α/β barrel, and is bordered by the N-terminal domain of the second subunit of the dimer. The active site is largely composed of a number of conserved charged residues that appear to be important for substrate binding and catalysis.

Conclusions: The seven-stranded α/β-barrel domain of QAPRTase is very similar in structure to the eight-stranded α/β-barrel enzymes. The structure shows a phosphate-binding site that appears to be conserved among many α/β-barrel enzymes including indole-3-glycerol phosphate synthase and flavocytochrome b2. The new fold observed here demonstrates that the PRTase enzymes have evolved their similar chemistry from at least two completely different protein architectures.

Addresses: [1]Department of Biochemistry, Albert Einstein College of Medicine, Bronx, NY 10461, USA and [2]Department of Biochemistry, Temple University School of Medicine, Philadelphia, PA 19140, USA.

[†]Present address: Department of Biochemistry and Biophysics, Texas A&M University, College Station, TX 77843-2128, USA.

*Corresponding author.
E-mail: sacchett@bioch.tamu.edu

Key words: α/β barrel, NAD biosynthesis, phosphoribosyltransferase, quinolinic acid, structure

Received: 16 September 1996
Revisions requested: 8 October 1996
Revisions received: 18 October 1996
Accepted: 21 October 1996

Electronic identifier: 0969-2126-005-00047

Structure 15 January 1997, 5:47–58

 ISSN 0969-2126

Introduction

Quinolinic acid phosphoribosyltransferase (QAPRTase; EC 2.4.2.19) is required for the *de novo* biosynthesis of NAD in both prokaryotes and eukaryotes [1]. The enzyme catalyzes the reaction between quinolinic acid (QA) and 5-phosphoribosyl-1-pyrophosphate (PRPP), to yield nicotinic acid mononucleotide (NAMN), pyrophosphate and CO_2, the latter resulting from decarboxylation at position 2 of the quinolinate ring (Fig. 1). QA is the first intermediate in *de novo* NAD synthesis that is common to all organisms, being produced via the degradation of tryptophan in most eukaryotes, and from dihydroxyacetone phosphate and L-aspartate in prokaryotes [1,2]. In addition to the *de novo* synthesis of NAD, salvage pathways exist (the purine nucleotide cycles or pncs) that allow recycling of NAD, usually via degradation of NAD in several steps to nicotinic acid (NA), followed by conversion of NA by nicotinic acid phosphoribosyltransferase (NAPRTase) to NAMN. In *Salmonella typhimurium* and *Escherichia coli*, neither QAPRTase nor NAPRTase can utilize the related substrate (NA or QA, respectively) at sufficient rates to sustain growth, pointing to high substrate specificity [3–5]. A lack of significant levels of NAPRTase activity in strains of *Mycobacterium tuberculosis* results in the secretion of NA, as NAD cannot be recycled, although the NAD degradation enzymes remain very active [1]. Thus, the *de novo* pathway of NAD biosynthesis may be a possible target for drug design against this organism.

QAPRTase has been grouped with nine other enzymes, (phosphoribosyltransferases, PRTases) that catalyze chemically similar phosphoribosyl transfer reactions using the substrate PRPP [6]. The PRTases are involved in *de novo* and salvage reactions of nucleotide synthesis, as well as in histidine and tryptophan biosynthesis. To date, crystal structures have been determined for several PRTase enzymes and all show a common 'PRTase fold' (the 'type I' fold) composed of a central parallel β sheet, of five

Figure 1

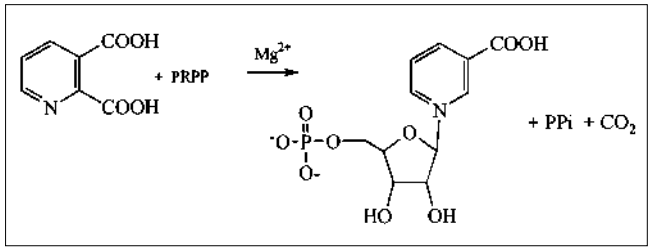

The reaction scheme of QAPRTase.

β strands, surrounded by α helices. The fold contains a common recognition motif of thirteen residues which is critical for PRPP binding and catalysis [7–11]. Typically, this 13-residue motif consists of four hydrophobic residues, followed by two acidic residues (usually aspartic acid), then two more hydrophobic residues and four smaller residues, including at least one glycine. The first four hydrophobic residues form the central β strand of the five-stranded β sheet. The two acidic sidechains lie in close proximity to the ribose group of the substrate and appear to be involved in the stabilization of a positively charged transition state [7,9]. The mechanism of nucleotide formation in hypoxanthine guanine PRTase (HGPRTase) and orotate PRTase has been proposed to proceed via a transition state which has oxocarbonium character at the ribose C1′–O4′ [12]. The four small residues at the end of the conserved motif serve to bind the 5′-phosphate of the PRPP and nucleotide.

Not all enzymes with PRTase activity show a convincing sequence corresponding to a type I PRPP-binding motif. In particular, QAPRTase [13], NAPRTase [14] and adenosine triphosphate PRTase do not appear to contain an obvious 13-residue motif. It is also surprising that QAPRTase shows little or no sequence similarity to NAPRTase, despite the almost identical reaction catalyzed by these two enzymes [13]. As these enzymes lack the type I PRPP-binding motif, it becomes possible that there might be at least two different types of PRTase fold. It is of interest to observe how a basically similar catalytic reaction can be undertaken by a different protein architecture, and specifically what motifs replace the dicarboxylate pair and phosphate-binding loop of the type I PRTase fold. In this paper, we present the three-dimensional (3D) structure of QAPRTase, which shows a new fold for a member of the PRTase group of enzymes. The active site and the residues likely to be involved in substrate binding and catalysis have also been identified.

Results and discussion

Overall fold of QAPRTase

A ribbon diagram of *S. typhimurium* QAPRTase is shown in Figure 2a, with a stereo diagram of the Cα trace shown in Figure 2b. The enzyme consists of two domains: an N-terminal openface sandwich domain comprising residues 8–135, and a C-terminal α/β barrel domain (residues 135–280). The C-terminal β strand (residues 284–296) forms a β sheet with the N-terminal domain β strand B1. The most striking and unexpected feature of the protein is the α/β barrel structure, which differs significantly from conventional eight-stranded α/β barrels, in following an $\alpha\beta\alpha\beta(\beta\alpha)_4\beta$ rather than $(\beta\alpha)_8$ topology.

The N-terminal domain is an antiparallel β openface sandwich structure comprised of a four-stranded β sheet stacked with four α helices. The bottom layer of the 'sandwich' is the four-stranded antiparallel β sheet consisting of β strands B1, B2, B3 and the end of the C-terminal β strand (B11; residues 285 to 296). Helices A2, A3 and A4 form the second layer of the sandwich. Typically, openface sandwich structures have been described as two-layer structures [15], but strictly the N-terminal domain of QAPRTase is a three layer sandwich, as the N-terminal long α helix (A1) stacks on top of helices A3 and A4. Strands B1 and B2 have short continuation β strands (B1a and B2a) located after a sharp bend, forming a short antiparallel two-stranded β sheet. The N-terminal domain ends with another long α helix, A4, which also marks the start of the α/β barrel.

The seven β strands of the α/β barrel are flanked by the C-terminal end of helix A4, and by only five additional helices. The resulting structure shows a large 'gap' between the second and third strands of the α/β barrel (strands B5 and B6), where there would be an additional β strand and two α helices in a normal $(\beta\alpha)_8$ structure. There is an additional short helix (A6a) between the βα unit of strand B6 and helix A6. Finally, instead of a final α helix after the last β strand of the barrel, strand B10 leads into a short α helix (A10) of 3–4 residues, then continues as the C-terminal β strand (B11; residues 285–296).

The QAPRTase α/β barrel

The QAPRTase α/β barrel is unlike any other α/β barrel structure reported to date. Although a seven β-stranded α/β barrel has been previously reported in the structure of cellobiohydrolase II (CBHII) [16], this differs in topology from QAPRTase. In CBHII, the gap between β strands occurs between the first and last strands of the barrel, whereas in QAPRTase, it occurs between the second (B5) and third (B6) β strands. In important respects, the QAPRTase barrel is like a conventional $\beta\alpha_8$ structure (and CBHII), having the same overall appearance, shear number (8) [17] and tilt angle (~35°) for the β strands. The absent β strand leaves a gap rather than compressing to an evenly spaced seven β-stranded barrel. There are no hydrogen bonds between strands B5 and B6, and these two strands lie nearly orthogonal to each other. The hydrogen bonding between strands B4 and B5, on

Figure 2

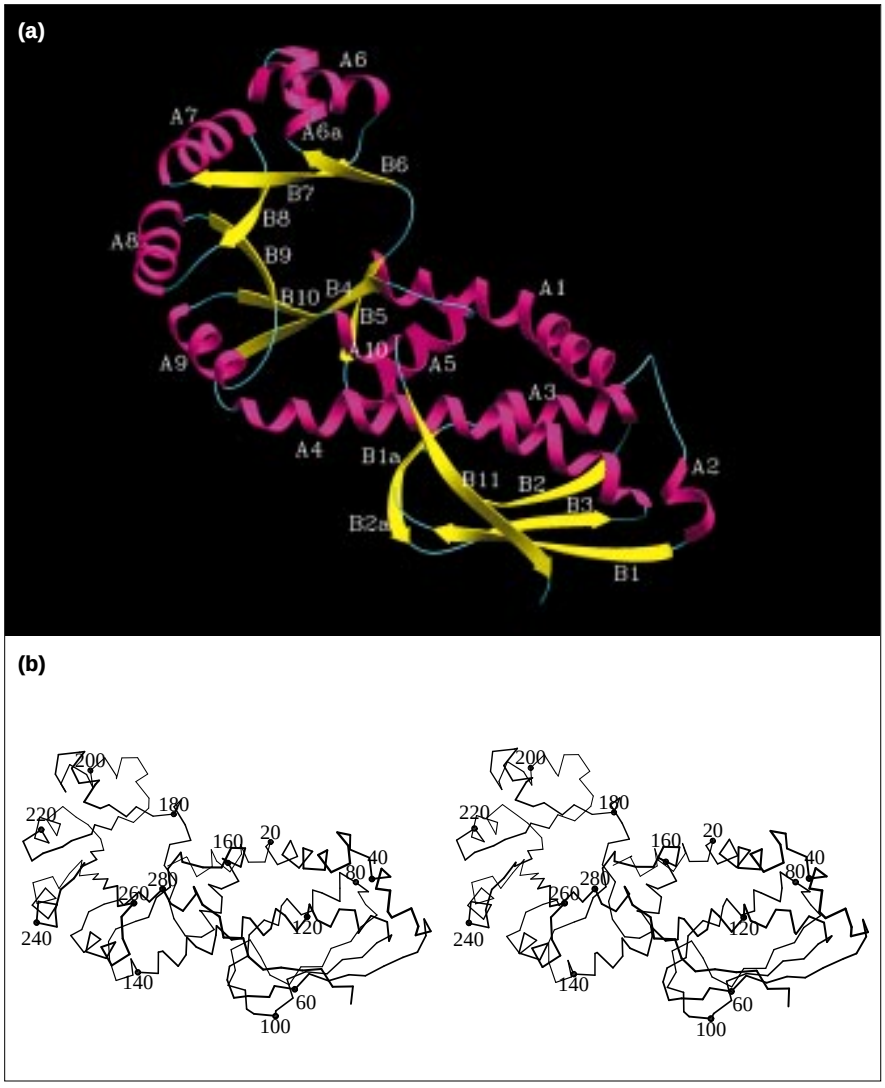

The overall fold of the QAPRTase monomer. (**a**) Ribbon diagram of the QAPRTase monomer. Secondary structure elements are sequentially labeled; helices are shown in magenta, β strands in yellow and loops in blue. (Figure prepared using SETOR [48].) (**b**) Stereo diagram of the Cα trace of the QAPRTase monomer; the positions of every twentieth residue are marked with a filled circle at the Cα position and are numbered. (Figure prepared using Molscript [49].)

one side of the gap is weaker than between the other strands; only one hydrogen bond is formed between these two β strands.

The α/β barrel of QAPRTase has an almost circular cross-section, like the α/β barrel of indole-3-glycerol phosphate synthase (IGPS; a subunit of the bifunctional enzyme *N*-5′-phosphoribosylanthranilate isomerase/IGPS) [18], and not as eliptical as triose phosphate isomerase [19]. Using the DALI algorithm for 3D structure comparisons [20], the highest scoring similar structures were: IGPS, *N*-acetylneuraminate lyase [21], the α subunit of tryptophan synthase, TRPS(α) [22], and flavocytochrome b2 [23], all of which have $(\beta\alpha)_8$ structures (Table 1). There does not seem to be any unifying functional relationship between QAPRTase and any of these structures, and thus the similarity is not likely to be of any particular significance to the reaction chemistry. However, it is interesting that several of the top scorers listed in Table 1 are enzymes that bind phosphate groups (see below).

Description of the dimer

S. typhimurium QAPRTase has been shown to exist as a dimer in solution [13]. A dimer was also observed in the asymmetric unit of the crystal (Fig. 3). The subunits are related by a non-crystallographic twofold axis ($\kappa = 179°$). The structure indicates that a dimer is essential for full activity of *S. typhimurium* QAPRTase, as the two subunits both contribute to the active site (see full description below). The two subunits are very similar, with a root mean square (rms) deviation of Cα atoms of 0.74 Å (for the QAPRTase–NAMN structure, the rms deviation is 0.56 Å). When the subunits are overlaid in the N-terminal domain, the region encompassing residues 180–206 of the

Table 1

Top nine matches of 3D structures with the α/β barrel of QAPRTase.*

Z score†	Rmsd (Å)††	LALI‡	Identity (%)§	Protein
8.8	3.4	137	15	Indole-3-glycerol phosphate synthase
7.9	3.7	139	9	*N*-Acetylneuraminate lyase
7.4	6.3	151	7	Flavocytochrome b2
7.1	3.5	137	15	TRPS(α)
6.4	3.4	92	8	Succinyl-CoA synthetase
6.3	3.5	134	6	Concanavalin B
5.4	3.6	138	8	β-Amylase
5.4	3.2	131	10	1,4-α-D-Glucan maltotetrahydrolase
5.3	4.0	136	11	Xylanase A catalytic core

*The DALI algorithm [20] was used to make the structural comparisons. †The Z score is the strength of structural similarity in standard deviations above expected. ††Positional root mean square deviation of equivalenced positions. ‡Length of entire chain of equivalenced structure. §Sequence identity of equivalent positions.

α/β barrel deviates by 2–3 Å between the non-crystallographic symmetry (NCS) related subunits (i.e. there is a shift of this segment of the α/β barrel). If residues 180–206 are omitted from the superposition, the rms deviation is only 0.54 Å for Cα atoms (0.32 Å for the QAPRTase–NAMN structure). Dimerization buries about 24% (2860 Å^2) of the surface area of each subunit. The dimer interface is fairly evenly distributed between charged or polar residues and hydrophobic residues.

Residues at the end of α helix A1, the following loop (residues 17–42), α helix A2, residues 154–157, residues 176–191 (containing B6 and A6a) and 284–288 (B11) are all involved in interactions at the dimer interface. There are a total of six hydrogen bonds at the dimer interface (Fig. 3). Two hydrogen bonds are formed between β strand B11 and its NCS mate, between the mainchain atoms of Val286 and its equivalent residue. Other hydrogen bonds are formed between sidechains Arg152 and Asp33, between the sidechain of Arg159 and the mainchain of Glu32, and between mainchain atoms in residues Asp33 and Leu178.

Description of the active site: QA binding

The QA molecule is located near the center of the α/β barrel, close to the C-terminal end of β strand B4. QAPRTase is similar to other α/β barrel enzymes in the location of the active site at the C-terminal ends of the β strands [24]. The active site is also bordered by the N-terminal domain of the other molecule of the dimer

Figure 3

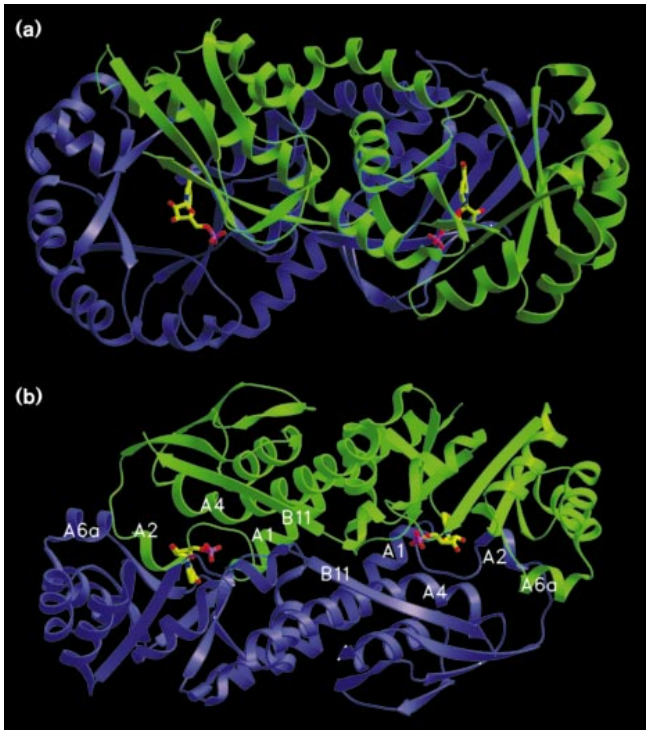

Two representations of the dimer of QAPRTase. (a,b) The two views are approximately orthogonal to one another. The figures show the backbone ribbon of QAPRTase and stick models of NAMN bound at the active sites. The two monomers are colored green and purple; secondary structure elements located at the dimer interface are indicated in (b).

(Fig. 3), which limits the solvent access to the QA (only 36 Å^2 of 151 Å^2 of the van der Waals surface of QA is exposed). At the resolution of the data, it was difficult to unambiguously orient the QA molecule. The orientation of QA shown in Figure 4 was deduced to be the most likely, based on the interactions with the protein and the appearance of 'omit' electron-density maps (Fig. 5). The 3-carboxylate group of QA is within hydrogen-bonding distance of the sidechain atoms Nε and Nη of Arg175 and Nε of Arg152, whereas the 2-carboxylate group only appears to hydrogen bond to the mainchain NH of Arg152. The 2-carboxylate group is ~4 Å from the sidechains of Lys153 and Arg118 (the latter residue from the N-terminal domain of the other molecule of the dimer). His174 is placed near C5 of the quinolinate ring and is also ~4 Å from the C3 carboxylate group. These sidechains create a basic pocket for the binding of the anionic substrate (Fig. 6). Leu183 and Thr151 are within van der Waals distance of the pyridine ring.

There are several differences in the active-site geometries in the two molecules of the QAPRTase dimer. In molecule A, Lys153 is 3.8 Å from the C2 carboxylate of QA,

Figure 4

Stereo diagram of the active site of QAPRTase showing bound QA. The QA molecule and amino acid sidechains at the active site are shown as a ball-and-stick representation; residues at the active site are labeled with the one letter code and their number. Arg118 is marked with an apostrophe to indicate that it is part of the other subunit of the dimer. Nitrogen and phosphorous atoms are shown in dark gray, carbon atoms are in white and oxygen atoms are in light gray.

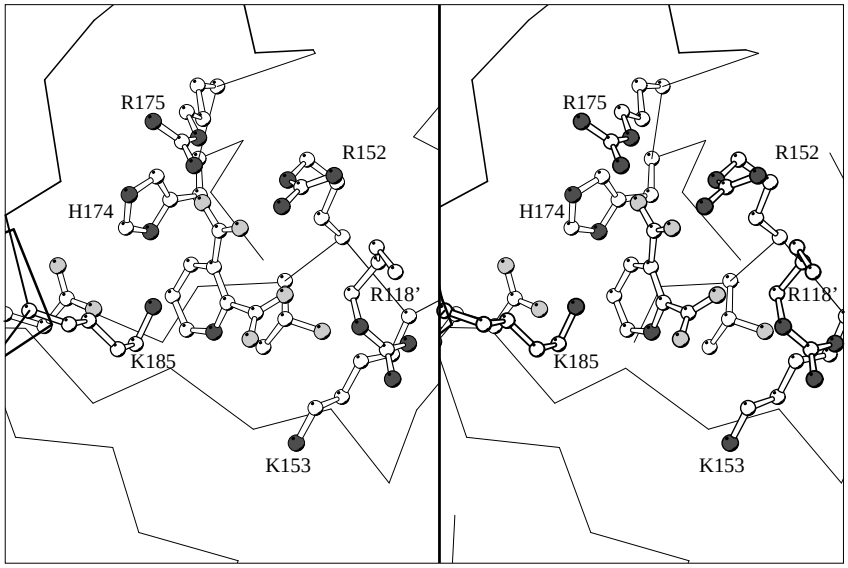

whereas the distance is >4 Å in molecule B. More significantly, the rigid-body shift of residues 180–206 (see above) between the two molecules places Lys185 much closer to the C2 carboxylate (~4 Å) in molecule B, compared to molecule A (>6 Å). This difference could explain the apparent lower occupancy of QA in the active site of molecule A.

A proposed mechanism for QAPRTase [5,25] involves the reaction of QA with PRPP to produce pyrophosphate and the hypothetical intermediate quinolinic acid mononucleotide (QAMN), which decarboxylates via an ylide to yield NAMN. It is not clear whether the decarboxylation of QAMN is spontaneous or enzyme assisted. The evidence for spontaneity of QAMN decarboxylation is based on the elevated rates of spontaneous decarboxylation observed for 1- and 3-substituted 2-pyridine carboxylic acids [26] and related pyrimidines [27], but enzymatic assistance of the decarboxylation seems quite plausible in QAPRTase. The positively charged residues close to the C2 and C3 carboxylate groups of QA are likely to stabilize the ylide intermediate, by both inductive electron withdrawal of negative charge from the pyridine ring via the C3 carboxylate, and by possible direct stabilization of negative charge at C2 by interaction with Lys185 or Arg118.

A negatively charged C2 substituent appears to be very important for the binding of QA. NA has no negative charge at position C2 and is not an inhibitor for *E. coli* and *S. typhimurium* QAPRTase, whereas several compounds with negative charges at this position have been shown to be effective inhibitors [5,28]. From the crystal structure, it is not clear exactly why such a strong preference is exhibited for a negatively charged group at C2, as there are more interactions with the C3 carboxylate than the C2 carboxylate. Arg118 and Lys185 could both move closer to the C2 position, and indeed the flexibility observed in the region (residues 180–206) could easily bring Lys185

Figure 5

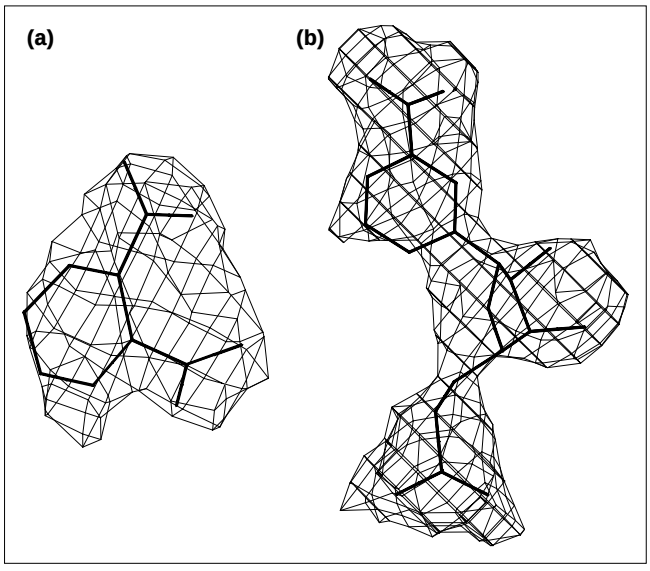

Electron density for ligands bound to QAPRTase. (**a**) Simulated annealing 'omit' electron-density map of the active site of the QAPRTase–QA complex, showing electron density (contoured at the 1σ level) for the bound QA. (**b**) Difference fourier map, $(|F_o|-|F_c|)\phi_c$, of the active site of the QAPRTase–NAMN complex. The map was calculated before addition of the NAMN coordinates to the model of QAPRTase, and shows clear electron density for the bound NAMN (final coordinates shown). The map is contoured at the 1.5σ level. (Figure generated using TOM [41].)

Figure 6

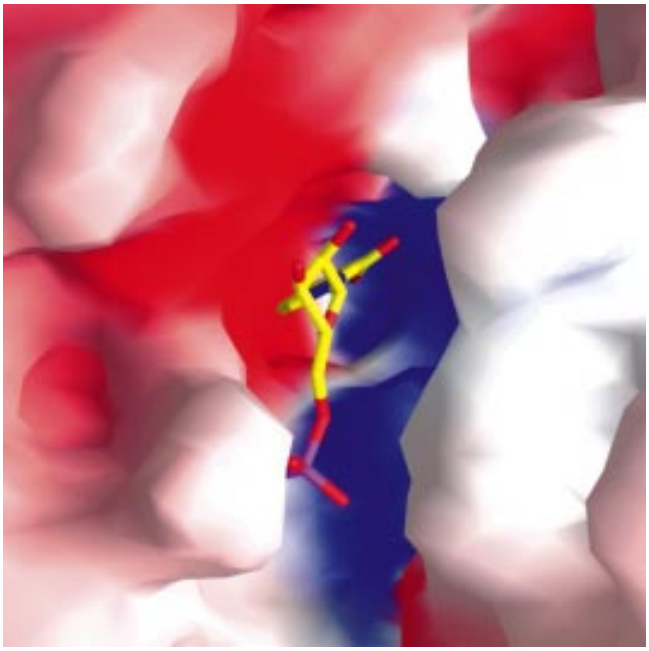

The active site of QAPRTase, showing bound NAMN in stick representation. The molecular surface of the protein is colored according to electrostatic potential: red = negatively charged, blue = positively charged. For the NAMN molecule, carbon atoms are shown in yellow, phosphorous in purple, oxygen in red and nitrogen in blue. (Figure generated using the program GRASP [50].)

to within hydrogen-bonding distance of the C2 carboxylate. Previous studies of multiply mutant strains of *S. typhimurium*, defective in the *de novo* and salvage pathways of NAD biosynthesis, indicated that Lys185 might play an important role in determining QAPRTase specificity. Mutant strains that could grow on NA rather than QA were all shown to contain mutations of QAPRTase at Lys185 (K Hughes, personal communication). However, Lys185 is not conserved in two of the nine aligned QAPRTase sequences (Fig. 7), casting some doubt on its importance in conferring specificity, unless these two sequences do not represent functional QAPRTases. (The *Rhodobacter capsulatus* and *Haemophilus influenzae* DNA sequences were identified as *nadC* genes on the basis of their sequence similarity with other *nadC* genes and not from functional data.)

Active site description: NAMN binding

Difference electron-density maps calculated with data extending to 3.0 Å resolution showed clear electron density for the two NAMN molecules bound to QAPRTase in the NAMN–QAPRTase complex (Fig. 5b); the two molecules of the QAPRTase dimer appear to bind NAMN with equal occupancy. The NA ring of NAMN occupies a very similar position to that of QA, and the ribose phosphate groups extend across the barrel towards β strands B9 and B10. The nicotinate ring is in an *anti* conformation, pointing away from the ribose phosphate group. Figure 8 shows the interactions of NAMN with QAPRTase. The ribose oxygens are within hydrogen-bonding distance of Lys185 Nζ and Asp235 Oδ1 and are almost within hydrogen-bonding distance to Glu214 Oε2 (3.65 Å). The phosphate group of NAMN makes interactions with the Nζ atoms of Lys153 and Lys284 and with mainchain nitrogens of Asn260 and Gly280. A structural adjustment in the area of residues 258–265 appears to accompany NAMN binding, as the 5′-phosphate group displaces the Asn260 sidechain from the position observed in the QA–QAPRTase complex. In the QA–QAPRTase complex, the sidechain of Asn260 partially occupies the phosphate-binding site and is within hydrogen-bonding distance to Gly280. On binding NAMN, the Asn260 sidechain moves away from the phosphate group (a shift of ~3 Å in the Cα position, further for the sidechain atoms) causing a 2–3 Å shift of the entire region of residues 260–265. Gly259 completely alters its position, with its backbone NH moving towards the phosphate oxygens, resulting in a Cα displacement of 4 Å. The conformation of residues 258–265 in the NAMN–QAPRTase complex is moderately clear from the electron density, whereas in the QA–QAPRTase complex there appears to be some disorder, with poorly defined density for residues Gly259, Asn260 and Val261.

Of the residues in the active-site area, most are strictly conserved in the nine aligned QAPRTase sequences (Fig. 7). Thr151, Arg152, Lys153, His174 and Arg175 are conserved in all nine known QAPRTase sequences, consistent with the interaction of Arg152 and Arg175 with the bound QA, and the interaction of Lys153 with the phosphate of NAMN. Arg118, which appears to be involved in intermolecular interactions with QA at the active site, is conserved as an arginine residue in seven out of nine sequences and is replaced by lysine in the remaining two sequences.

In the ribose-binding site, Glu214 is conserved in all nine aligned sequences and Asp235 is conserved in eight of nine, changing to glutamatic acid in the *R. capsulatus* sequence. These two acidic residues near the ribose oxygens are strongly reminiscent of the two catalytically essential and highly conserved acidic residues in the type I PRTases. Several studies have shown that the transition states for enzymatic phosphoribosyl transfer are oxycarbonium-like [12,29], and a transition state structure with a high degree of oxycarbonium ion character has been deduced for the reaction catalyzed by orotate PRTase [12]. By analogy to the mechanisms proposed for orotate PRTase and HGPRTase [9], Glu214 and Asp235 are likely to be involved in the stabilization of a positively charged transition state in QAPRTase. Activation of the ribose towards transition state formation might also include deprotonation at the

Figure 7

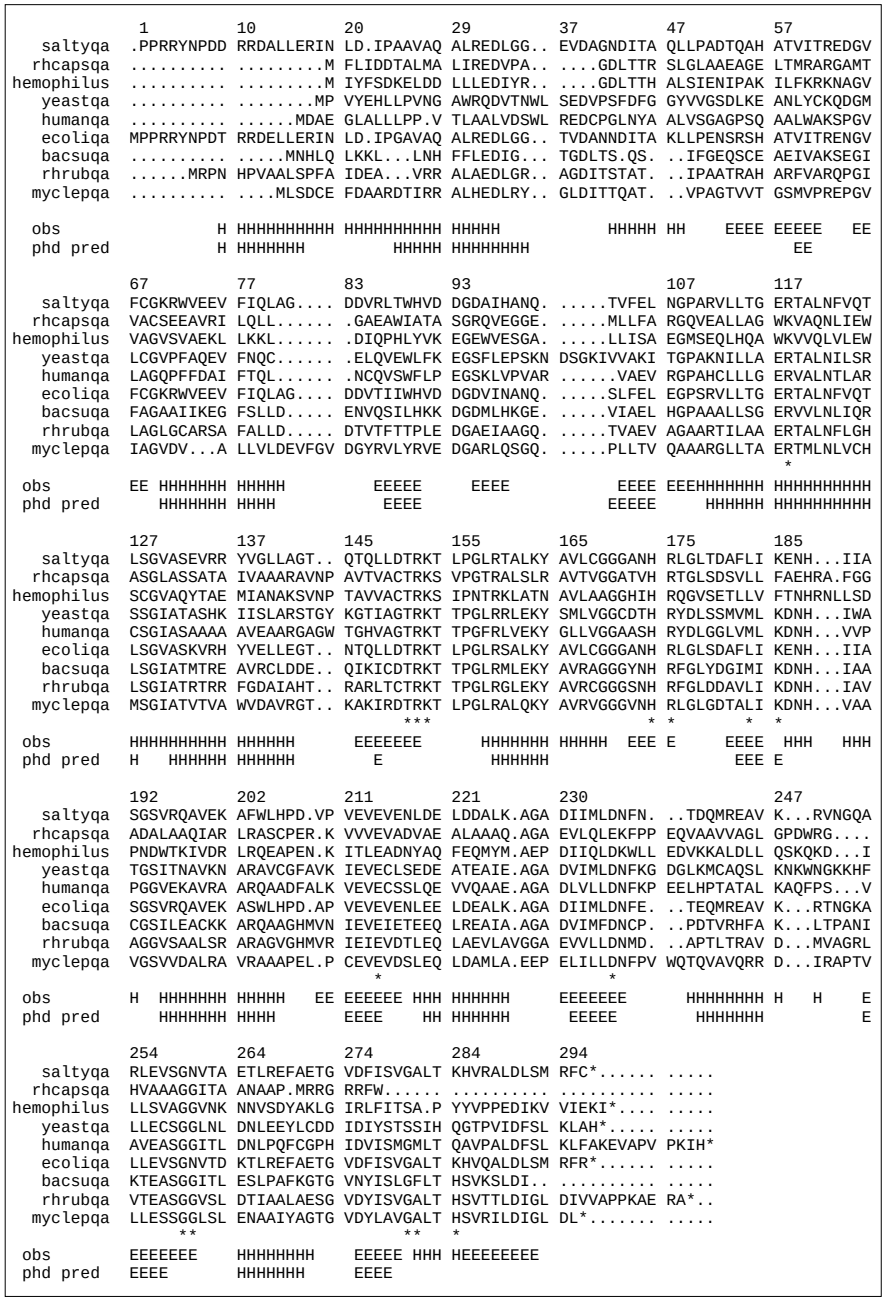

Alignment of QAPRTase sequences showing observed (obs) and predicted (phd pred; predicted by PHD server [44,45]) secondary structure. Helical (H) and β strand (E) structures are indicated. For the predicted secondary structure, only the prediction with estimated accuracy of > 82 % is indicated. Asterisks mark residues that are found at the active site. Sequences are, from top to bottom: *Salmonella typhimurium* (saltyqa); *Rhodobacter capsulatus* (rhcapsqa); *Haemophilus influenzae* (hemophilus); *Saccharomyces cerevisiae* (yeastqa); human (humanqa); *Escherichia coli* (ecoliqa); *Bacillus subtilis* (bacsuqa); *Rhodospirillum rubrum* (rhrubqa); and *Mycobacterium leprae* (myclepqa).

2′-hydroxyl group and protonation of the leaving pyrophosphate. In QAPRTase, Glu214 is well positioned to undertake d eprotonation of the 2′-hydroxyl. Potential proton donating residues lining the putative pyrophosphate-binding site of QAPRTase include Lys153 and Lys185.

The phosphate-binding site provides the least conserved region, in terms of sequence identity. As stated above, Lys153 is conserved in all nine sequences, but Lys284 only occurs as a lysine residue in two; this residue is a histidine in three of the aligned sequences and a glutamine in two. In the two most divergent sequences, this position is either 'missing' (*R. capsulatus*) or replaced by tyrosine (*H. influenzae*). The contacts with mainchain atoms (Asn260, Gly280) will be preserved despite sidechain changes, but in fact both position 260 and 280 are commonly glycine residues in QAPRTase sequences (Fig. 7). In fact, the entire phosphate-binding 'structure' appears to be conserved amongst phosphate-binding enzymes with α/β barrel structures (see below).

Figure 8

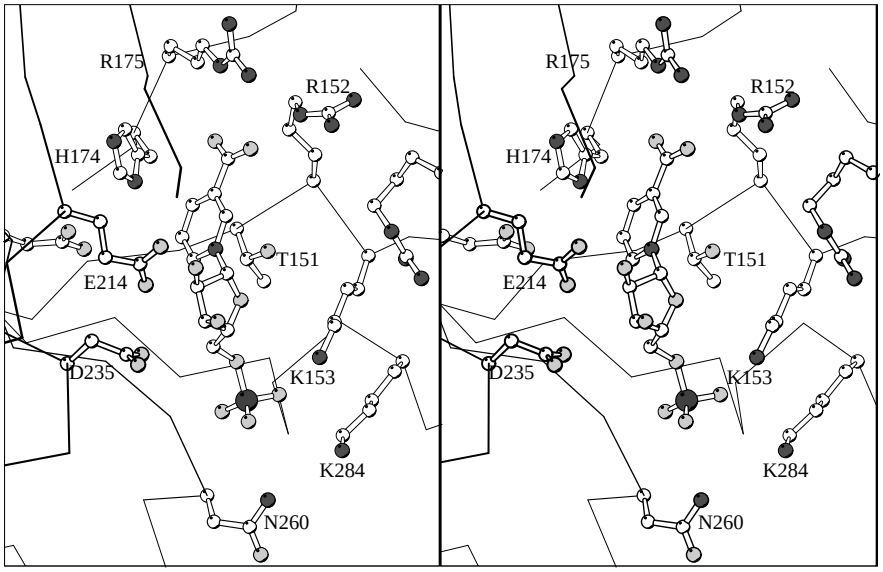

Stereo diagram of the active site of QAPRTase showing bound NAMN. NAMN is shown in ball-and-stick representation; atoms are labeled and colored as described in Figure 4.

The conserved phosphate-binding motif in α/β barrel structures

The results from the alignment of similar 3D protein structures placed IGPS and flavocytochrome b2 as top scorers in their degree of 3D similarity to the QAPRTase α/β barrel (Table 1). Inspection of the aligned structures revealed that, when the 3D structures are aligned using the β strands of the α/β barrel, the phosphate moieties bound to these two enzymes superimposed very well with the 5′-phosphate of NAMN bound to QAPRTase (Fig. 9). The appearance of this phosphate-binding motif in at least eight α/β barrel enzymes has been discussed [30]. In this group of structures, the phosphate group is bound between the C-terminal ends of the final two β strands of the α/β barrel (i.e. between β strands 7 and 8 of conventional α/β barrel structures and between β strands B9 and B10, the last two β strands, of the QAPRTase α/β barrel). The sequence conservation amongst the phosphate-binding motifs is poor, but the structures overlay in quite a striking manner (Fig. 9). There is almost no conservation of the basic residues that coordinate the phosphate group; Lys153 (conserved in QAPRTase) is equivalent to Lys55 in IGPS, but has no exact counterpart in flavocytochrome b2. Not surprisingly, Lys284, which is not conserved in QAPRTase, is not observed in IGPS or the other phosphate-binding α/β barrels. The short helix of residues 280–284 (helix A10) in QAPRTase corresponds to the additional helix (α8′) in flavocytochrome b2, IGPS and TRPS(α).

QAPRTase and the other PRTases: a new fold for the PRTase family

QAPRTase is the only known PRTase structure to contain an α/β barrel fold. Orotate PRTase, HGPRTase and glutamine-PRPP amidotransferase all have a similar type I PRTase fold, consisting of five parallel β strands surrounded by four α helices [7–9]. These PRTases contain a conserved motif of 13 residues [7,9,31] that serves to bind the ribose-phosphate moiety of the substrate PRPP and is found at the center of the PRTase fold.

Figure 9

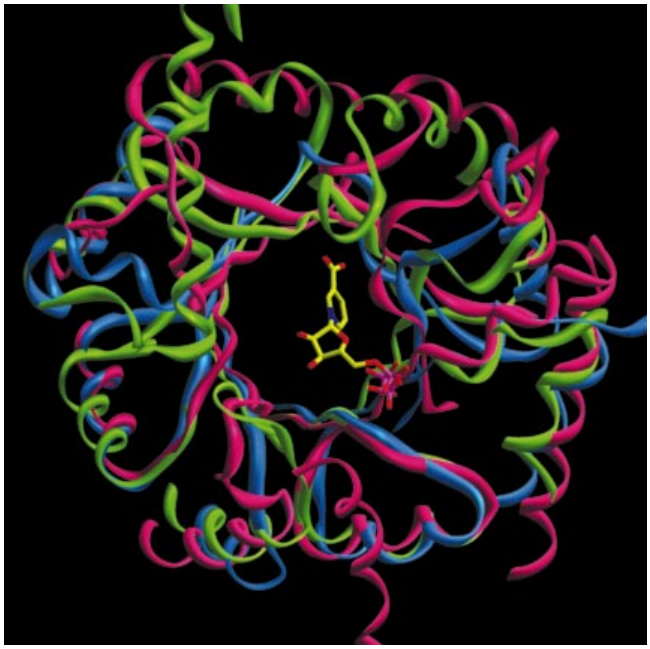

Overlay of the phosphate-binding site regions of QAPRTase (in blue), flavocytochrome b2 (in magenta) and indole-3-glycerol phosphate synthase (in green). The bound NAMN is shown in stick form with atom coloring as in Figure 6.

This motif does not appear in QAPRTase, being replaced by residues from several different parts of the structure. There are two acidic amino acid residues near the ribose oxygens of the substrate, Glu214 and Asp235, but unlike the type I PRTases, these residues are not adjacent in sequence either to each other or to the phosphate-binding site. The phosphate-binding site is a completely different structure in QAPRTase, being composed of several different entities rather than a continuous loop of five residues. The phosphate-binding regions provided by QAPRTase appear to form a conserved motif amongst α/β barrel enzymes (see below).

Other PRTases of unknown structure show the 13-residue motif (e.g. adenine PRTase and uracil PRTase), and will most likely assume the type I PRTase fold of orotate PRTase and HGPRTase. However, NAPRTase also lacks the 13-residue 'PRPP-binding' motif [14], suggesting that this enzyme may also lack the type I PRTase fold. It is interesting that a $(\beta\alpha)_8$ structure has been predicted for anthranilate PRTase [32], which contains an Asp-Glu-x-x-x-x-Gly-x-Thr sequence, which is reminiscent of the conserved motif of the type I PRTases, but is not clearly conserved as in other type I PRTases.

In summary, the structure of QAPRTase is unusual in two ways. Firstly, the structure is an irregular α/β barrel, having only seven β strands, and only six surrounding helices. However, the phosphate-binding motif has been previously observed in a number of apparently unrelated α/β barrel enzymes. This may suggest that QAPRTase is evolutionarily related to these enzymes, possibly having evolved from an ancestral $(\beta\alpha)_8$ structure with a phosphate-binding site. Secondly, QAPRTase is the first PRTase to deviate from the five-β-stranded PRPP-binding motif exhibited by HGPRTase, orotate PRTase, and glutamine-PRPP amidotransferase. This observation shows that members of the PRTase group of enzymes have evolved convergently to perform similar functions utilizing different protein architecture.

Biological implications

Quinolinic acid phosphoribosyltransferase (QAPRTase) catalyzes the formation of nicotinic acid mononucleotide (NAMN) from the substrates quinolinic acid (QA) and phosphoribosyl pyrophosphate (PRPP). It is an essential enzyme for the *de novo* synthesis of NAD. Quinolinic acid (QA) is produced in most prokaryotes from the condensation of aspartic acid and dihydroxyacetone phosphate. In animals the degradation of tryptophan produces QA, which is also a known neurotoxin. QA has been shown to be present at high levels in the central nervous systems of patients with a broad spectrum of inflammatory neurological diseases, including HIV-1 and meningitis [33,34]; it has been proposed that the elevated QA levels may be responsible for causing significant neurological damage in these patients. The high QA levels may arise from an increase in indoleamine-2,3-dioxygenase activity, the first step in the kynurenine tryptophan degradation pathway [33]. QA is known to bind to *N*-methyl-D-aspartate receptors, and may cause damage by overstimulation of these receptors [35]. QAPRTase provides the only route for the metabolism of QA.

In addition to its importance in the metabolism of QA and its role in NAD biosynthesis, QAPRTase is of interest as a member of the group of phosphoribosyltransferases (PRTases) that utilize the substrate 5-phosphoribosyl-1-pyrophosphate (PRPP). Structures of several PRTases have now been published, and all show a common fold of five **β** strands surrounded by four **α** helices. The lack of sequence similarity between QAPRTase and the other PRTases was suggestive of a different three-dimensional structure for this enzyme.

The three-dimensional structure of QAPRTase from *Salmonella typhimurium* consists of two domains: an N-terminal domain, containing a four-stranded **β** sheet and four **α** helices in an antiparallel openface sandwich structure, and a C-terminal domain which is a seven-stranded **α/β** barrel. The different structure observed for QAPRTase implies that it must have evolved from a different ancestor than other PRTases. The substrates bind to the **α/β** barrel with the carboxylate groups of QA located in a very cationic binding pocket, containing conserved arginine, lysine and histidine residues. The 5′-phosphate group of the product NAMN is located between the last two **β** strands of the barrel, in a phosphate-binding site that is extremely similar to those observed in other phosphate-binding **α/β** barrels, such as flavocytochrome b2 and indole-3-glycerol phosphate synthase.

Materials and methods

Materials

Buffers, reagent grade chemicals, and luria broth (LB) media were obtained from Sigma. PEG-400 and $MgCl_2$ for crystallizations were obtained from Fluka. DEAE Toyo-Pearl ion exchange resin was from Toso-Haas. Plasmid pSP73 and plasmid purification kits were obtained from Promega, and restriction enzymes were supplied by New England Biolabs. Polymerase chain reaction (PCR) reagents were purchased from Perkin Elmer.

Preparation of QAPRTase

Plasmid pAD01 [12] was used as a template for PCR amplification of the 900 bp *nadC* gene. The primers used (5′ GTTTTATCATAGC-CGCCCTCGC 3′ and 5′ CATCGGCTGCAGAGGATCAGC 3′, base changes underlined) introduced an *Nde*I site immediately 5′ of the start codon, and a *Pst*I site five bp 3′ of the stop codon. PCR products were purified using a kit for this purpose (Promega), digested with *Nde*I and *Pst*I, gel purified, and ligated into pSP73 (Promega) previously cut with the same enzymes. The resultant plasmid, designated pDOQA01, was used to transform BL21(DE3) [36], yielding strain DOQA100. DNA sequencing insured that no adventitious mutations had occurred in *nadC* during PCR. For large scale (12×500 ml) growth, cells from a freshly prepared and centrifugally washed overnight culture were used to inoculate LB broth and the cultures allowed to grow with shaking

until $A_{550\,nm} = 0.8$ was reached. At this time isopropyl-β-D-thiogalactopyranoside (IPTG) (0.4 mM final) was added, and growth allowed to continue for 3 h. The cells were harvested by centrifugation, washed, and resuspended in two volumes of buffer Q (0.1 M Tris, brought to pH 8.0 with H_3PO_4, and containing 1 mM EDTA and 2.5 mM dithiothreitol (DTT). Cells were stored at –20 °C.

S. typhimurium QAPRTase was isolated from DOQA100 following the procedure of Hughes *et al.* [13] with modifications and additional chromatographic steps. All steps were conducted at 0–4 °C, except for the chromatography which was performed at room temperature. Following thawing of cells, phenylmethyl sulfonyl fluoride was added to 1 mM from a 0.3 M stock in isopropanol, and sonication was carried out for three 1 min bursts at full power. After centrifugation at 12 000 rpm for 20 min, the supernatant was treated with 30 ul ml^{-1} of 10 % polyetheneimine, pH 8.0, and stirred for 15 min. The supernatant was centrifuged, and the pellet dissolved in a minimal volume of buffer Q. The solution was dialyzed overnight against three changes of buffer Q. Particulate matter was removed by centrifugation, and the solution applied to a column (2.5 × 25 cm) of DEAE-Toyo-Pearl resin. The column was eluted at a flow rate of 3 ml min^{-1} with a linear gradient of 0–0.5 M Na_2SO_4 in buffer Q using a Pharmacia FPLC apparatus. Fractions exhibiting QAPRTase activity emerged at 45 % of the gradient, and were pooled and reprecipitated with 65 % saturation $(NH_4)_2SO_4$. The protein was redissolved in 0.1 M potassium phosphate buffer, pH 7.2 containing 1 mM EDTA and 2.5 mM DTT (buffer QKP), and dialyzed against three changes of the same buffer overnight. The dialyzed protein was then rechromatographed on DEAE-Toyo-Pearl resin, using buffer QKP and a linear gradient of 0–0.5 M Na_2SO_4. Fractions containing activity were pooled, precipitated with 65 % saturation $(NH_4)_2SO_4$, redissolved in 4 ml of buffer QKP containing 0.5 M Na_2SO_4 and applied to a column (1.6 × 10 cm) of phenyl sepharose (Pharmacia), equilibrated with the same buffer. The column was eluted at a flow rate of 3 ml min^{-1} with a descending linear gradient of 0.5–0 M Na_2SO_4. Fractions containing QAPRTase eluted at about 9.5 % of the gradient and were pooled and brought to 65 % saturation $(NH_4)_2SO_4$ and stored at 4 °C. The protein was homogeneous as judged by 15 % SDS PAGE. The enzyme was assayed as described [13], and showed a specific activity of 0.9 U mg^{-1}.

Crystallization of QAPRTase

The initial crystallization conditions were found by a sparse matrix screening method (Crystal Screen I, Hampton Research, CA). Crystals of QAPRTase were prepared using the hanging-drop vapor diffusion method. Recombinant *S. typhimurium* QAPRTase at 20–30 mg ml^{-1} in buffer (20 mM Tris, pH 8, 0.05 % NaN_3, 2 mM DTT, 2 mM QA) was mixed 1:1 with a precipitant solution of 25–30 % PEG 400, 0.1 M Hepes pH 7.1–7.5 and 0.2 M $MgCl_2$, and suspended over 1 ml of the same precipitant solution. Typically crystals appeared after a few days, and grew to maximum dimensions of 0.5 × 0.2 × 0.2 mm within one month. The crystals diffract to a maximum resolution of 2.6 Å. To produce crystals with bound NAMN, apo-QAPRTase was crystallized using the same precipitant solution described above (i.e. without QA in the hanging drop). The apo-QAPRTase crystals were soaked for 24 h in mother liquor containing 2 mM NAMN immediately prior to data collection.

Data collection and processing

X-ray data were collected at room temperature using a Siemens area detector, with a Rigaku RU-200 rotating anode as the X-ray source. Data were processed using the program XENGEN [37]. The unit cell dimensions were determined to be $a = b = 81.4$ Å, $c = 217.3$ Å, $\alpha = \beta = \gamma = 90°$. The space group was determined from pseudo-precession pictures [38] to be either $P4_12_12$ or $P4_32_12$. The asymmetric unit contains a dimer of QAPRTase and 54 % solvent. The two molecules in the asymmetric unit are related by an approximate twofold axis ($\kappa = 179$), which was calculated from the Hg and Ir atom positions, then later recalculated after model building. Heavy-atom derivatives were prepared by soaking QAPRT–QA co-crystals in a mother liquor containing 28 % PEG 400, 0.1 M Hepes pH 7.1, 0.2 M $MgCl_2$, and heavy-atom concentrations in the range 1–3 mM. Derivatives that were used in phase calculations were obtained using ethylmercuriphosphate (EMP, 3 mM), mercuric acetate (1–2 mM), Sm(III)acetate (1.5 mM), Nd(III)acetate (2 mM), K_2IrCl_6 (3 mM). The results of data collection and phasing are summarized in Table 2.

Structure determination and refinement

Isomorphous difference Patterson maps were used to locate the mercury atom positions in the EMP and mercuric acetate (MA) derivatives. Trial protein phases were calculated from the mercury atom positions [38], then other derivatives were located using difference Fourier maps. The space group was determined to be $P4_12_12$ (as opposed to its enantiomer $P4_32_12$) by use of the anomalous scattering of the iridium derivative [39]. The final figure of merit for the phase set calculated before solvent flattening was 0.62. Protein phases were calculated [38] to 3.0 Å, and solvent flattening and histogram matching were employed to improve the phases [40]. The resulting electron-density map was mostly interpretable, showing clear regions of continuous electron density, to which a polyalanine chain was fitted using the program TOM [41]. There were several breaks in the polyalanine chain and very poor electron density for the N-terminal domain of each monomer. One cycle of real-space averaging (RAVE [42]) of the electron density was undertaken, using a manually edited solvent mask (MAMA [43]) and the non-crystallographic symmetry matrix calculated from an incomplete model (2928 atoms, or 66 % of atoms). The resulting map allowed the remaining polypeptide chain in the N-terminal region to be fitted. The alignment of the amino acid sequence onto the

Table 2

QAPRTase structure determination and heavy-atom derivative data.

Data set	Number of sites	Redundancy* of data	Maximum resolution (Å)	R_{sym}†	R_{merge}‡	Phasing power§	Completeness (%)
Native–QA	–	5.3	2.8	0.12	–	–	93
K_2IrCl_6	5	3.2	3.0	0.13	0.07	1.09 (0.81)	93
EMP††	2	2.5	3.3	0.12	0.09	1.33	86
Hg acetate	2	2.8	3.0	0.11	0.08	1.48 (1.25)	88
Nd acetate	4	2.5	3.2	0.10	0.09	0.81	94
Sm acetate	4	2.3	3.5	0.11	0.10	0.76	94

*Number of observations/number of unique reflections. †Unweighted absolute R factor on intensity: $R = \Sigma | I - < I > | / \Sigma I$, where I is the observed intensity of a reflection, and $< I >$ is the mean intensity of the reflection. ‡Merging R factor (on F) with the native data set: $R = (\Sigma |F_{PH} - F_P|) / \Sigma F_P$, where F_P and F_{PH} are the native and protein + heavy-atom structure factor, respectively. §Phasing power is the ratio of the root mean square (rms) calculated heavy-atom structure amplitude to the rms lack of closure. The values in parentheses are for the anomalous diffraction data. ††EMP = ethylmercuriphosphate derivative.

Table 3

Heavy-atom binding sites in QAPRTase.

Heavy atom	Protein ligand(s)††
Hg (EMP)*	CysA168
Hg acetate*	CysA168, CysA68
Pt1*†	HisA56, CysB296
Pt2†	MetA233, GluA214
Sm1, Nd1	GluA220, GluB220‡, GluA216
Sm2, Nd2	GluB220, GluB216
Sm3, Nd3	AspA223, AspB223‡
Sm4, Nd4	AspB512, AspA240
Ir1*	In QA-binding site
Ir2*	In phosphate-binding site
Ir3	B291 C = O (mainchain), LysA153, GlnB125: in active-site area at dimer interface

*Sites were observed at equivalent positions in the NCS related molecule. †The Pt derivative was obtained by soaking a QAPRTase crystal overnight in mother liquor containing 4 mM K_2PtCl_4; sites were located in difference Fourier maps but were not used for phasing. ††The letter A or B refers to different monomers of the QAPRTase dimer observed in the asymmetric unit of the crystal. ‡Indicates symmetry related molecule. (Details of the derivatives are given in the text.)

polyalanine chain was deduced by inspection of the electron density, the observed heavy-atom binding sites (Table 3) and the predicted secondary structure [44,45]. As sidechains were fit into the electron density, new electron-density maps were calculated using combined model and heavy-atom phases.

Model building to phase combined electron-density maps resulted in an initial model of 3774 protein atoms (558 of 592 residues) which was refined by molecular dynamics and energy minimization (X-PLOR [46]) with non-crystallographic restraints, using data to 2.8 Å. At all stages of refinement, the R_{free} was monitored for continued decreases as more refinable parameters were introduced. At the resolution available, the observation : parameter ratio is approximately 1:1 when all atoms and temperature factors are refined, leading to the possibility of over fitting of the data. Monitoring the R_{free} allowed us to judge that the refinement was improving the model. The initial model had an R factor of 45.3 %, which dropped to 26.3 % (R_{free} = 40.7 %) after refinement. Three further cycles of manual model building, using $(3|F_o|-2|F_c|)\phi_c$ and $(|F_o|-|F_c|)\phi_c$ maps and energy minimization refinement, were employed. Two further cycles of model building and refinement using least squares methods [47] were performed, followed by one final round of simulated annealing ('slowcooling' from 3000 K) and energy minimization (using non-crystallographic restraints on mainchain atoms only), followed by individual temperature-factor refinement. Difference Fourier maps clearly revealed the location of bound QA, and this was added to the model. Further cycles of model building and alternating positional and B factor refinement in X-PLOR resulted in a final R factor of 18.2 %, and R_{free} of 27.4 % (Table 4). Non-crystallographic restraints were removed in the final cycles of refinement. Both the conventional R factor and R_{free} continued to drop after the restraint was released. A solvent mask correction (X-PLOR) was employed during the final stages of refinement, using solvent parameters and refinement protocol optimized by D Kostrewa (Hoffman LaRoche). Six solvent atoms were added to the model at positions of well defined peaks of electron density (at least 3σ) in the $(|F_o|-|F_c|)\phi_c$ difference map, and where hydrogen-bonding partners with the protein were available within 3.5 Å.

The final model is a dimer (the subunits are labeled A and B; residues of each subunit are labeled A8–A296 and B8–B296). Each subunit of the dimer contains 289 of 296 residues (4444 total protein atoms in dimer). There are also two molecules of QA and six solvent atoms.

Table 4

Summary of final statistics.

	QAPRTase–QA	QAPRTase–NAMN
Resolution (Å)	2.8	3.0
No. of crystals	2	1
R_{sym} (%)*	11.9	10.6
$< I / I >$	6.3	5.8
No. of unique reflections	17 451	13 925
Redundancy	5.3	2.9
Completeness (%)	92.7	90.7
R factor (%)†	18.6	19.9
R_{free} (%)††	27.4	32.3
Rms deviation bond lengths (Å)	0.01	0.015
Rms deviation bond angles (°)	1.7	2.0

*R_{sym} = unweighted absolute R factor on intensity: $R = \Sigma | I - < I > | / \Sigma I$, where I is the observed intensity of a reflection, and $< I >$ is the mean intensity of the reflection. †The R factor reported is for the data with $I / \sigma I > 2$. ††R_{free} = R factor for a test set of reflections not used during refinement (10 % of QAPRTase–QA data and 5 % of QAPRTase–NAMN data).

One molecule of QA (molecule A) has been modeled at 50 % occupancy, as the electron density in difference maps was weak and initial modeling at 100 % occupancy resulted in unreasonably high temperature factors for the molecule. The first seven residues of each monomer are omitted from the model, as the electron density is poorly defined. The rms deviations from ideal geometry are 0.010 Å for bond lengths and 1.7 for bond angles. The average B factor for all atoms is 45.9 $Å^2$, rather higher than is typical. The average B factor for mainchain atoms of the α/β barrel of molecule A is 40 $Å^2$. The high overall B factor probably reflects the poor quality of the data collected at high resolution rather than any intrinsic disorder in the crystal structure. There is one outlier in the Ramachandran plot, Asn250 (and its NCS equivalent), which is located within a loop of three residues between helix A8 and β strand B9. Simulated annealing omit maps calculated in this region confirmed the overall conformation of this loop. The heavy-atom positions were found to fall next to appropriate sidechains in the QAPRTase structure (Table 3). In addition, there was good agreement of the observed secondary structure with the predicted secondary structure (Fig. 7). Simulated annealing omit maps (X-PLOR) were made over all of the model, and confirmed the structure.

For the structure of QAPRTase complexed with NAMN, the refined QAPRTase coordinates without ligand or solvent were subjected to rigid-body refinement, followed by simulated-annealing refinement using X-PLOR (using data to 3.0 Å). Simulated annealing omit maps and $(3|F_o|-2|F_c|)\phi_c$ maps were calculated, and the area around the active site (in particular residues 250–270) were rebuilt. Alternating energy minimization and group B factor refinement reduced the R factor to 21.3% (R_{free} = 33.4 %), and difference electron-density maps clearly showed two molecules of NAMN bound to the QAPRTase dimer (Fig. 5b). The ligands were added to the model, and further model building at the active site, followed by energy minimization and group B factor refinement reduced the R factor to 19.9 % (R_{free} = 32.4 %). The final statistics for the QAPRTase–NAMN structure are summarized in Table 4.

Accession numbers

The coordinates of the QAPRTase–QA structure have been deposited with the Brookhaven database, the accession code is 1QAP.

Acknowledgements

The authors are grateful to Dr S Roderick and Dr G Scapin for their expert advice. This work was supported by grant GM48623 from the NIH.

References

1. Foster, J.W. & Moat, A.G. (1980). Nicotinamide adenine dinucleotide biosynthesis and pyridine nucleotide cycle metabolism in microbial systems. *Microbiol. Rev.* 44, 83–105.
2. Tritz, G.J. (1987). NAD biosynthesis and recycling. In *Escherichia coli and Salmonella typhimurium: Cellular and Molecular Biology, Vol. 1*. (Neidhart, F.C., Ingraham, J.L., Low, K.B., Magasanik, B., Schaechter, M. & Umbarger, H.E., eds), pp. 557–563, American Society for Microbiology, Washington D.C., USA.
3. Penfound, T. & Foster, J.W. (1995). Biosynthesis and recycling of NAD. In *Escherichia coli and Salmonella: Cellular and Molecular Biology, Vol. 1*. (Neidhart, F.C., ed.), pp. 721–730, American Society for Microbiology, Washington D.C., USA.
4. Foster, J.W., Kinney, D.M. & Moat, A.G. (1979). Pyridine nucleotide cycle of *Salmonella typhimurium*: isolation and characterization of *pncA*, *pncB* and *pncC* mutants and utilization of exogenous nicotinamide adenine dinucleotide. *J. Bacteriol.* 137, 1165–1175.
5. Kallikin, L. & Calvo, K. (1988). Inhibition of quinolinate phosphoribosyltransferase by pyridine analogs of quinolinic acid. *Biochem. Biophys. Res. Commun.* 152, 559–564.
6. Musick, W.D. (1981). Structural features of the phosphoribosyltransferases and their relationship to the human deficiency disorders of purine and pyrimidine metabolism. *Crit. Rev. Biochem.* 11, 1–34.
7. Scapin, G., Grubmeyer, C. & Sacchettini, J.C. (1994). Crystal structure of orotate phosphoribosyltransferase. *Biochemistry* 33, 1287–1294.
8. Smith, J.L., *et al.*, & Satow, Y. (1994). Structure of the allosteric regulatory enzyme of purine biosynthesis. *Science* 264, 1427–1433.
9. Eads, J.C., Scapin, G., Xu, Y., Grubmeyer, C. & Sacchettini, J.C. (1994). The crystal structure of human hypoxanthine-guanine phosphoribosyltransferase with bound GMP. *Cell* 78, 325–331.
10. Smith, J.L. (1995). Enzymes of nucleotide biosynthesis. *Curr. Opin. Struct. Biol.* 5, 752–757.
11. Schumacher, M.A., Carter, D., Roos, D.S., Ullman, B. & Brennan, R.G. (1996). Crystal structures of *Toxoplasma gondii* HGXPRTase reveal the catalytic role of a long flexible loop. *Nat. Struct. Biol.* 3, 881–887.
12. Tao, W., Grubmeyer, C. & Blanchard, J.S. (1996). Transition state structure of *Salmonella typhimurium* orotate phosphoribosyltransferase. *Biochemistry* 35, 14–21.
13. Hughes, K.T., Dessen, A., Gray, J.P. & Grubmeyer, C. (1993). The *Salmonella typhimurium nadC* gene: sequence determination by use of Mud-P22 and purification of quinolinate phosphoribosyltransferase. *J. Bacteriol.* 175, 479–86.
14. Vinitsky, A., Teng, H. & Grubmeyer, C. (1991). Cloning and nucleic acid sequence of the *Salmonella typhimurium pncB* gene and structure of nicotinate phosphoribosyltransferase. *J. Bacteriol.* 173, 536–540.
15. Richardson, J.S. (1981). The anatomy and taxonomy of protein structure. *Adv. Protein Chem.* 34, 167–339.
16. Rouvinen, J., Bergfors, T., Teeri, T., Knowles, J.K.C. & Jones, T.A. (1990). Three-dimensional structure of cellobiohydrolase II from *Trichoderma reesei*. *Science* 249, 380–386.
17. McLachlan, A.D. (1979). Gene duplications in the structural evolution of chymotrypsin. *J. Mol. Biol.* 128, 49–79.
18. Wilmanns, M., Priestle, J.P., Niermann, T. & Jansonius, J.N. (1992). Three-dimensional structure of the bifunctional enzyme phosphoribosyl-anthranilate isomerase: indoleglycerolphosphate synthase from *Escherichia coli* refined at 2.0 Å resolution. *J. Mol. Biol.* 223, 477–507.
19. Banner, D.W., *et al.*, & Waley, S.G. (1975). Structure of chicken muscle triose phosphate isomerase determined crystallographically at 2.5 Å resolution using amino acid sequence data. *Nature* 255, 609–614.
20. Holm, L. & Sander, C. (1993). Protein structure comparison by alignment of distance matrices. *J. Mol. Biol.* 233, 123–138.
21. Izard, T., Malby, R.L., Lawrence, M.C., Lilley, G.G. & Colman, P.M. (1994). The three-dimensional structure of *N*-acetylneuraminate lyase from *Escherichia coli*. *Structure* 2, 361–370.
22. Hyde, C.C., Ahmed, S.A., Padlan, E.A., Miles, E.W. & Davies, D.R. (1988). Three-dimensional structure of the tryptophan synthase $\alpha_2\beta_2$ multienzyme complex from *Salmonella typhimurium*. *J. Biol. Chem.* 263, 17857–17871.
23. Xia, Z. & Mathews, F.S. (1990). Molecular structure of flavocytochrome b2 at 2.4 Å resolution. *J. Mol. Biol.* 212, 837–847.
24. Brändén, C.-I. (1980). Relation between structure and function of α/β proteins. *Q. Rev. Biophys.* 13, 317–338.
25. Bhatia, R. & Calvo, K.C. (1996). The sequencing, expression, purification and steady-state kinetic analysis of quinolinate phosphoribosyltransferase from *Escherichia coli*. *Arch. Bioch. Biophys.* 2, 270–278.
26. Dunn, G.E. & Thimm, H.F. (1976). Kinetics and mechanism of decarboxylation of some pyridinecarboxylic acids in aqueous solution. *Can. J. Chem.* 55, 1342–1347.
27. Beak, P. & Siegel, B. (1976). Mechanism of decarboxylation of 1,3-dimethylorotic acid. A model for orotidine 5′-phosphate decarboxylase. *J. Am. Chem. Soc.* 98, 3601–3606.
28. Mann, D.F. & Byerrum, R.U. (1974). Quinolinic acid phosphoribosyltransferase from castor bean endosperm 1: purification and characterization. *J. Biol. Chem.* 249, 6817–6823.
29. Chelsky, D. & Parsons, S. (1975). Stereochemical course of the adenosine triphosphate phosphoribosyltransferase reaction in histidine biosynthesis. *J. Biol. Chem.* 250, 5669–5675.
30. Wilmanns, M., Hyde, C.C., Davies, D.R., Kirschner, K. & Jansonius, J.N. (1991). Structural conservation in parallel α/β barrel enzymes that catalyse three sequential reactions in the pathway of tryptophan biosynthesis. *Biochemistry* 30, 9161–9169.
31. Hershey, H.V. & Taylor, M.W. (1986). Nucleotide sequence and deduced amino acid sequence of *Escherichia coli* adenine phosphoribosyltransferase and comparison with other analogous enzymes. *Gene* 43, 287–293.
32. Wilmanns, M. & Eisenberg, D. (1993). Three-dimensional profiles from residue-pair preferences: identification of sequences with α/β barrel fold. *Proc. Natl. Acad. Sci. USA* 90, 1379–1383.
33. Heyes, M.P., *et al.*, & Tourtellotte, W.W. (1992). Quinolinic acid and kyurenine pathway metabolism in inflammatory and non-inflammatory neurological disease. *Brain* 115, 1249–1273.
34. Saito, K., Nowak, T.S. Jr., Markey, S.P. & Heyes, M.P. (1993). Mechanism of delayed increases in kyurenine pathway metabolism in damaged brain regions following transient cerebral ischemia. *J. Neurochem.* 60, 180–192.
35. Foster, A.C., Gill, R. & Woodruff, G.N. (1988). Neuroprotective effects of MK-801 *in vivo*: selectivity and evidence for delayed degeneration mediated by NMDA receptor activation. *J. Neurosci.* 8, 4745–4754.
36. Studier, F.W., Rosenberg, A.H., Dunn, J.J. & Dubendorff, J.W. (1990). Use of T7 polymerase to direct expression of cloned genes. *Methods Enzymol.* 185, 60–89.
37. Howard, A.J. (1986). A guide to data reduction for the nicolet imaging proportional counter: the XENGEN system. Genex Corporation, Gaithersburg, MD, USA.
38. Furey, W. & Swaminathan, S. (1990). PHASES. *Am. Cryst. Assoc. Annu. Mtg. Program. Abstr.* 18, 73.
39. McRee, D. (1993). Practical protein crystallography. Academic Press, NY, USA.
40. Cowtan, K. (1994). DM: CCP4 density modification package, release 1.5. Joint CCP4 and ESF-EACBM Newsletter on Protein Crystallography 31, 34–48.
41. Jones, T.A. (1985). Interactive computer graphics: FRODO. *Methods Enzymol.* 115, 157–171.
42. Jones, T.A. (1992). *Molecular Replacement*. (Dodson, E.J., *et al.*, eds), pp. 92–105, SERC Daresbury Laboratory, Warrington, UK.
43. Kleywegt, G.J. & Jones, T.A. (1993). MAMA. *ESF/CCP4 Newsletter* 28, 56–59.
44. Rost, B. (1996). PHD: predicting one-dimensional protein structure by profile based neural networks. *Methods Enzymol.* 266, 525–539.
45. Rost, B. & Sander, C. (1993). Prediction of protein secondary structure at better than 70 % accuracy. *J. Mol. Biol.* 232, 584–599.
46. Brünger, A.T. (1992). *X-PLOR, Version 3.1. A system for X-ray Crystallography and NMR*. Yale University Press, New Haven, CT, USA.
47. Tronrud, D.E., Ten Eyck, L.F. & Matthews, B.W. (1988). An efficient general purpose least-squares refinement program for macromolecular structures. *Acta Cryst. A* 43, 489–501.
48. Evans, S.V. (1993). SETOR: hardware lighted three dimensional solid model representation of macromolecules. *J. Mol. Graph.* 11, 134–138.
49. Kraulis, P.J. (1991). MOLSCRIPT: a program to produce both detailed and schematic plots of protein structures. *J. Appl. Cryst.* 24, 946–950.
50. Nicholls, A., Sharp, K. & Honig, B.H. (1991). Protein folding and association: insights from the interfacial and thermodynamic properties of hydrocarbons. *Proteins* 11, 281–296.